1   *Article*

2   # MRI study of the influence of surface coating aging
3   # on the *in vivo* biodistribution of iron oxide
4   # nanoparticles

5   **Susana Carregal-Romero** [1, 2, *, †]**, Sandra Plaza-García** [3, †]**, Rafael Piñol** [4]**, Jose Luís Murillo** [4]**,**
6   **Jesús Ruiz-Cabello** [1, 2, 5, 6]**, Daniel Padro** [3]**, Angel Millán** [4] **and Pedro Ramos-Cabrer** [3, 5, *]

8   [1]   Molecular and Functional Biomarkers group, CIC biomaGUNE, Donostia-San Sebastián, Spain
9   [2]   CIBER de Enfermedades Respiratorias (CIBERES), Madrid, Spain
10   [3]   Magnetic Resonance Imaging Laboratory, CIC biomaGUNE, Donostia-San Sebastián, Spain
11   [4]   CSIC-Universidad de Zaragoza, ICMA, Zaragoza, Spain
12   [5]   Ikerbasque, Basque Foundation for Science, Bilbao, Spain
13   [6]   Universidad Complutense de Madrid, Madrid, Spain

14   *   Correspondence: pramos@cicbiomagune.es, scarregal.ciberes@cicbiomagune.es; Tel.: +34-943-005-426

15   †   These authors have contributed equally to this work

17   **Abstract:** Medical imaging is an active field of research that fosters the necessity for novel
18   multimodal imaging probes. In this line, nanoparticle-based contrast agents are of special interest,
19   since those can host functional entities either within their interior, reducing potential toxic effects of
20   the imaging tracers, and on their surface, providing high payloads of probes, due to their large
21   surface-to-volume ratio. The long-term stability of the particles in solution is an aspect usually
22   under-tackled during probe design in research laboratories, since their performance is generally
23   tested briefly after synthesis. This may jeopardize a later translation into practical medical devices,
24   due to stability reasons. To dig into the effects of nanoparticle aging in solution, respect to their
25   behavior *in vivo*, iron oxide stealth nanoparticles were used at two stages (3 weeks *vs.* 9 months in
26   solution), analyzing their biodistribution in mice. Both sets of nanoprobes showed similar sizes,
27   zeta potentials and morphology, as observed by DLS and TEM but, fresh nanoparticles
28   accumulated in the kidneys after systemic administration, while aged ones accumulated in liver
29   and spleen, confirming an enormous effect of particle aging on their *in vivo* behavior, despite barely
30   noticeable changes perceived on a simple inspection of their structural integrity.

31   **Keywords:** iron oxide nanoparticles; multimodal nanoparticles; biodistribution; magnetic
32   resonance imaging; aging; coating degradation.

34   ## 1. Introduction

35       Medical imaging is seeking to overcome inherent limitations regarding sensitivity, specificity,
36   resolution and scanning time, by means of acquisition of multimodal images. This has motivated the
37   development of novel scanners able to combine several imaging techniques (e.g. positron emission
38   tomography and magnetic resonance imaging -PET/MRI- scanners), and the growth of a research
39   field focused on the fabrication of multimodal imaging probes (contrast agents). In this line,
40   Magnetic Resonance Imaging (MRI) is a non-invasive imaging technique with superb capacity to
41   image soft tissues at high resolution and contrast, regardless of the depth within the body. Because
42   of its inherent relatively low sensitivity, in comparison with other imaging techniques (e.g. nuclear
43   imaging), and to speed up acquisition times, an important research activity exists around MRI,

44   aiming at producing MRI contrast agents. Those agents usually combine their magnetic properties
45   with other physical properties (e.g. fluorescence or radioactive decay) for multimodal imaging
46   purposes [1-4]. In this context, iron oxide nanoparticle (IONP)-based contrast agents seem ideal
47   [5-6], first, because of their already proven effectiveness as MRI contrast agents [7-8]. Indeed, the use
48   of IONPs as MRI contrast agents started 20 years ago, becoming very popular due to their ability to
49   dramatically reduce T2 relaxation times in organs such as liver, spleen and bone marrow, by
50   selective uptake and accumulation in cells belonging to the mononuclear phagocyte or
51   reticuloendothelial system (RES). In second place, because nanoparticles have the capacity of being
52   labeled with other imaging probes, both on their surface, via chemical bonding or chelation within a
53   coordination complex and, in their interior, by doping the crystalline structure [9-12]. The fabrication
54   of multimodal nanoparticles based on the chemical functionalization of their organic coating is
55   nowadays skeptically accepted, because several studies have shown the loss of such coatings in
56   organic fluids, or by enzymatic degradation *in vivo* [13-15]. Therefore, the alternative doping of iron
57   oxide nanocrystals with other probes, such as ^{111}In or ^{64}Cu, is gaining more interest, and the number
58   of novel synthetic protocols has risen in the last years [3, 10, 16, 17]. In this way, the integrity of the
59   nanoparticle and the multimodal imaging function can be secured.

60   As important as keeping the integrity of the nanoparticles is the prediction and control of their
61   fate for the effective application in nanomedicine. The choice of the administration route is one of the
62   major factors that affects biodistribution. Intravenous injection (IV) is the most commonly used route
63   for IONPs in MRI. Unfortunately, most of "naked" IONPs intravenously injected are rapidly filtered
64   out by the mononuclear phagocyte system (MPS) also known as reticuloendothelial system (RES),
65   reducing their efficacy for diagnosis [18]. The RES formed by monocytes and macrophages
66   eliminates pathogens or foreign bodies, such as IONPs, by phagocytosis. The elimination process
67   involves three steps: (a) opsonization, where plasma proteins deposit on the surface of the IONPs,
68   (b) recognition by macrophages and (c) phagocytosis which consists on the engulfment of the IONPs
69   for subsequent degradation and metabolism. Therefore, liver and spleen are the major clearance
70   pathways for the IONPs from blood, unless high doses are injected to cause the saturation of these
71   organs, and accumulating the excess of the IONPs in other parts of the RES [19]. Fortunately, IONPs
72   can be tailored (i.e. we can modulate surface coating, shape, etc.) to increase their blood circulation
73   times by making them stealth to the RES system [20-22].

74   Nanoparticles' size is one of the most important factors determining the biodistribution routes
75   and kinetics. IONPs with a diameter larger than 100 nm tend to accumulate in liver and spleen,
76   while nanoparticles smaller than 10-15 nm are normally eliminated by renal clearance [21, 23, 24].
77   Nanoparticles with a diameter between 10 and 100 nm have, in principle, longer blood circulation
78   times, making possible the access to other tissues or organs [25, 26].   In order to ensure an uniform
79   biodistribution, IONPs should have low polydispersity index (PDI), but more importantly, size
80   stability is highly required to avoid any type of aggregation [27, 28], which is sometimes caused by
81   inappropriate surface coating [29]. Nanoparticle aggregates are quickly trapped by the RES. [30]
82   Among the different types of coatings, polyethylene glycol (PEG) is the most widely used, providing
83   stability to the IONPs via steric hindrance, as well as excellent anti-fouling properties, decreasing
84   blood and serum protein interactions, which subsequently minimizes opsonization, macrophage
85   uptake and RES clearance, increasing the blood circulation time of the IONPs [31, 32].

86   Here we report the influence of the long term stability of PEG coating on the biodistribution of
87   grape shaped iron oxide nanoparticles, designed as dual contrast agents for MRI and SPECT
88   imaging. We have recently reported the synthesis of these particles by the co-precipitation of
89   ^{111}In-doped magnetic nanoparticles, and their further coating with polyethylene glycol [17]. We
90   describe the effect of aging of those nanoprobes in solution, relating the physicochemical
91   modifications suffered by the particle with the changes in their *in vivo* biodistribution in mice, as
92   determined by MRI. A set of freshly prepared nanoparticles (3 weeks in solution) was compared to
93   an aged batch (circa 9 months in solution). Both sets of particles showed similar size distributions,
94   zeta potentials and morphology, as observed by DLS and transmission electron microscopy (TEM),
95   but after systemic administration in mice, the freshly prepared particles accumulated mostly in the

96  kidneys, while the aged ones mostly accumulated in liver. Our results demonstrate how even small
97  changes at structural level may have a radical influence on the *in vivo* behavior of nanomaterials.
98

99  **2. Materials and Methods**

100      *2.1 Synthesis of grape shaped IONPs*
101      The preparation of IONPs and further PEG coating was carried out by a first step of formation
102  of poly(4-vinyl pyridine) (P4VP) coated maghemite via co-precipitation, and a final PEG coating via
103  the formation of pyridine-acrylate bonds through a Michael reaction, with acrylated PEG ligands.
104  The grape shape is obtained during the PEG coating step. In this work ^{111}In was not included in the
105  synthesis, as previously described [17], since only the MRI imaging modality was used to analyze
106  the biodistribution of the nanomaterials. The different batches were prepared following exactly the
107  same protocol, being the post-synthesis aging in solution (3 weeks vs. circa 9 months) the only
108  difference between them. Further detailed information about the synthesis procedure is provided in
109  previous work [17].
110

111      *2.2 Sample characterization*
112      The concentration of iron in each sample has been determined by atomic absorption with ion
113  coupled plasma mass spectrometry (40 ICP Perkin-Elmer spectrometer). A LaB6-TEM, type JEOL
114  JEM-1400PLUS (40kV - 120kV) equipped with a GATAN US1000 CCD camera (2K x 2K) was used to
115  image iron oxide nanoparticles. A ζ-Sizer Malvern Instrument was used for the Dynamic Light
116  Scattering measurements. All studies were performed in backscattering mode at a 173° scattering
117  angle, with temperature controlled at 25 °C.
118

119      *2.3 Relaxometry measurements*
120      *In vitro* characterization of MR properties of the IONPs was performed prior to *in vivo* studies,
121  determining their longitudinal and transverse relaxivities (r1 and r2, respectively). These
122  measurements were carried out at 37 ºC on a Bruker Minispec MQ60 instrument (Bruker Biospin
123  GmbH, Ettlingen, Germany). All experiments were performed using a total volume of 300 μl of
124  sample (ca. 0.12 mM iron concentration) to prepare a series of dilutions, using HPLC grade water as
125  solvent. Longitudinal (T1) and transverse (T2) relaxation times were determined using the
126  inversion-recovery and the CPMG methods, respectively. T1 and T2 relaxation times allowed us to
127  determine the corresponding relaxivities (r1 and r2) fitting the relaxation rate (R1 and R2)
128  dependence of the concentration using the following equation:

$$R1,2 = (1/T1,2) = R1,2_0 + r1,2\ [CA], \tag{1}$$

129      where $R1_0$, $R2_0$, R1 and R2 are the relaxation rates before and after contrast agent, [CA] is the
130  concentration of the contrast agent, and r1 and r2 are the magnetic relaxivities.
131

132      *2.4 Magnetic Resonance Imaging (MRI)*
133      MRI *in vivo* studies were performed using a 7 T horizontal bore Bruker Biospec USR 70/30 MRI
134  system (Bruker Biospin GmbH, Ettlingen, Germany), interfaced to an AVANCE III console, and with
135  a BGA12-S imaging gradient insert (maximal gradient strength 400 mT/m, switchable within 80 μs).
136      Animal experiments were conducted in our institutional animal facility, which holds a full
137  accreditation from the Association for the Assessment and Accreditation of Laboratory Animal Care
138  International (AAALAC). All animal procedures were approved by our Institutional animal care
139  and use committee (IACUC), and local authorities (Diputación Foral de Guipuzcoa, Spain).
140      For the *in vivo* studies a group of n=6 and a group of n=7 eight-weeks old BALB/cJRj female mice
141  (21.2 ± 2 g body weight; Janvier, France) were used to test the biodistribution of the aged and fresh
142  IONPs, respectively.
143      Imaging was achieved with a 40 mm inner diameter volume-coil working in quadrature for
144  both, signal transmission and reception. Animal preparation was started by inducing anesthesia

145  with 5% isoflurano (reduced to 2-3% during image acquisition), in a 35/65% mixture of $O_2/N_2$ a
146  carrier gas. The tail vein was catheterized (PE catheter attached to a 30G needle) for the posterior
147  intravenous injection of the contrast agent inside of the magnet.  Animals were prevented from
148  hypothermia with the use of a water blanket, maintaining the temperature at 37±1 ºC. To ensure
149  animal welfare, temperature and respiration rate were continuously monitored while they remain in
150  the MRI magnet, using a SAII M1030 system (Small animal instruments, NY, USA), also used to
151  synchronize image acquisition with the respiration of the animal. MRI scanning started with
152  baseline scans prior to the injection of the IONPs. Then, 100 µl of contrast agent (200 µg/ml of Fe in
153  NaCl 0.007 M and pH 7.5) was injected to the animals inside the magnet, acquiring MR images up to
154  120 min post injection, in intervals of 20 min. Anatomical T1-weighted axial and coronal images
155  were acquired pre and post-injection of the contrast agent with a FLASH (Fast Low Angle Shot)
156  sequence (TE = 4 ms; respiration synchronized (TR = 600 ms); FA = 30º; NA = 2; Matrix = 256 x 256
157  points; FOV = 40 x 40 mm; spatial resolution = 156 x 156 um; 20-24 slices of 1 mm thickness covering
158  the major extension of the organs of interest at abdominal level). For quantification, T2 maps were
159  acquired using a MSME (multi-slice multi-echo) pulse sequence (20 echoes equally spaced, ranging
160  TE = 8-160 ms with ΔTE = 8 ms); TR = 3 x respiration rate (~60 breaths per min giving a TR~3 s); NA =
161  2; Matrix = 160 x 160 points; FOV = 24 x 24 mm; spatial resolution = 150 x 150 um; 8-12 slices of 1 mm
162  thickness in 2 slice packages, one covering the kidneys/spleen region and the other the liver region).

163
164      *2.5 In vivo MRI Quantification*
165      T2 parametric maps were generated on a pixel-by-pixel basis fitting the acquired images to a 3
166  parameter exponential decay using the Levenberg-Margardt method:

$$S = C + S_0 \exp(-TE/T2), \tag{2}$$

167  where $S_0$ represent the signal intensity (S) at echo time TE = 0 ms, C is an offset, and TE is the
168  independent variable (echo time). All image fittings have been performed with customized routines
169  for the NIH image-J software. Mean differences in T2 relaxation times ($\Delta T2 = T2_t - T2_{\text{pre-contrast}}$) were
170  calculated for each time-point (t), in manually selected regions of interest (ROIs: liver, spleen,
171  kidney's cortex and kidney's medulla). For the analysis, all the slices where the organ of interest was
172  visible were included, giving a representative bulk value for T2 for each of the analyzed organs. It
173  should be emphasized that pixels in these regions presenting large T2 values, corresponding to
174  fluids such as blood or bile (gallbladder and bile ducts in the liver, and large blood vessels in the
175  liver and kidneys) were excluded from the quantitative analysis. Thus, a maximal cutoff threshold
176  level for T2 was set to 30, 20 or 50 ms for the liver, spleen and kidneys, respectively. These values are
177  beyond a safe limit of mean +2 SD (standard deviation of the mean) for each organ.
178

179  **3. Results and Discussion**

180      3.1. Influence of aging ion the physicochemical properties of the grape shaped IONPs

181      Grape shaped iron oxide nanoparticles were produced as described elsewhere [17]. Figure 1
182  shows a schematic representation of the two different steps of the synthesis protocol. First, single
183  and small iron oxide nanoparticles with an average diameter of 3.8 nm were produced, followed by
184  polyethylene glycol coating by pyridine acrylate bonding to the surface of the nanoparticles.

185

186

187

188

189
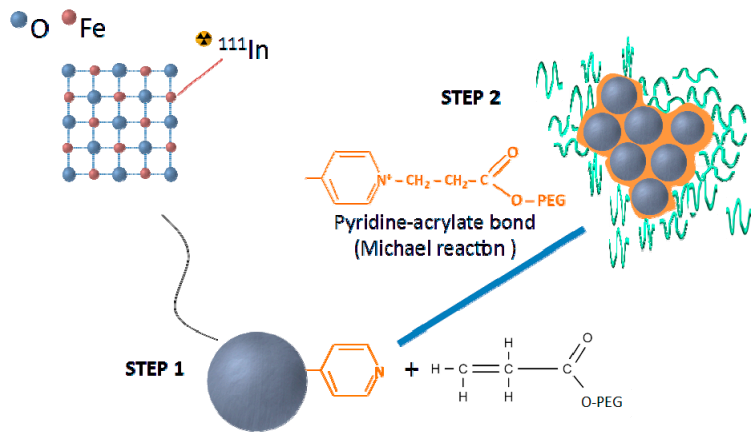
**Figure 1.** Schematic representation of the synthetic protocol of the IONPs. During STEP 1 small single IONPs are formed by coprecipitation and coated with P4PV. STEP 2 corresponds to the surface functionalization with acrylate terminated PEGs through a Michael reaction with P4PV.

IONPs were characterized by transmission electron microscopy after different times in solution, following synthesis. Freshly prepared solutions (3 weeks in solution) were compared to aged ones (circa 9 months in solution). Figure 2B and 2C show TEM images of the 2 sets of nanoparticles, founding no significant differences between them, with similar sizes and degree of agglutination observed for both sets. Dynamic light scattering (DLS) was also used to determine the hydrodynamic diameter of the samples (Figure 2D), showing no significant differences between fresh (52.1 nm) and aged solutions (55.9 nm). Measurement of the zeta potentials also resulted in no significant differences (26.0±0.4 *vs.* 24.1±0.3 mV) between the two sets of nanoparticles, demonstrating that the charge of the nanoparticles was not significantly influenced by the time that nanoparticles remained in solution.
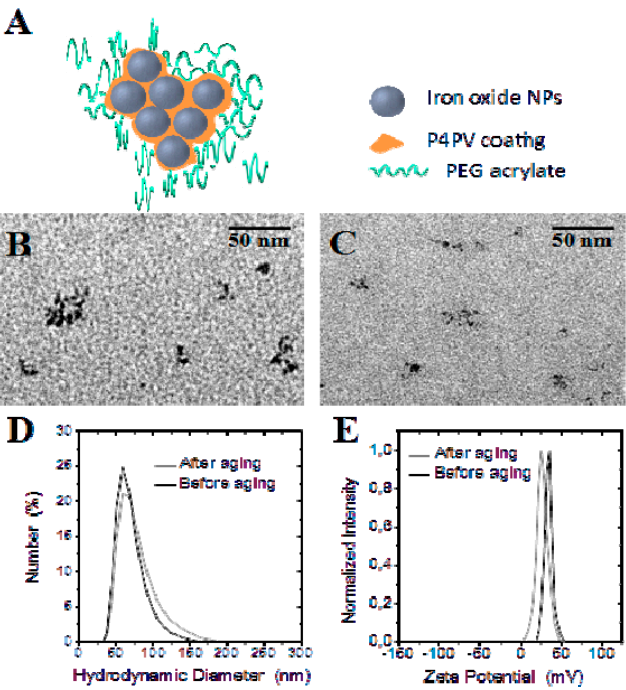


**Figure 2.** A) Schematic representation of IONPs and their components. TEM images of freshly prepared IONPs (B) compared with aged IONPs (C). Hydrodynamic diameter (d, in nm) of fresh (black line) *vs.* aged (grey line) solutions. (E) Zeta potential (in mV) of fresh (black line) and aged (grey line) IONPs' solutions.

229     3.2. MR Relaxometry

230     Relaxometry measurements of the IONPs for different dilutions allowed us to represent the
231     dependence of the relaxation rates (R1 and R2) with iron concentration (Figure 3).



232
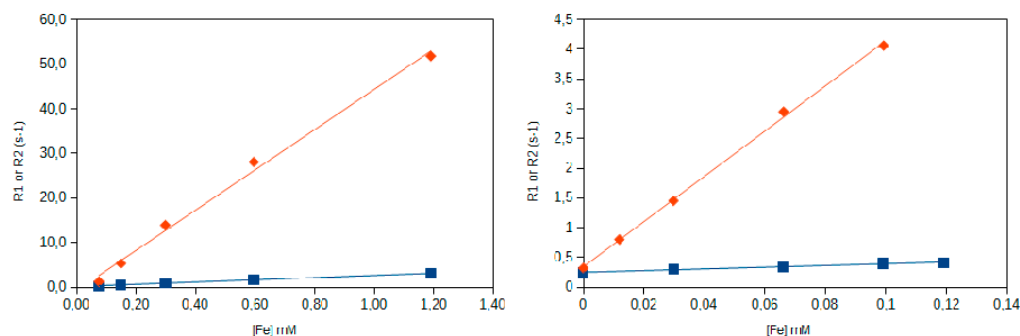
233     **Figure 3.** Variation of the longitudinal (R1, blue squares) and transverse (R2, red diamonds)
234     relaxation rates (the reciprocal of T1 and T2 relaxation times) with iron concentration (as determined
235     by ICP-mass) for the aged left, and freshly prepared (right) solutions of nanoparticles, at 1.41 T.

236

237     The corresponding relaxivities found for the contrast agent where $r1 = 1.42$ mM(Fe)$^{-1}$s$^{-1}$ and $r2 =$
238     $38.0$ mM(Fe)$^{-1}$s$^{-1}$ for the freshly prepared solution and $r1 = 2.5$ mM(Fe)$^{-1}$s$^{-1}$ and $r2 = 45$ mM(Fe)$^{-1}$s$^{-1}$ for
239     the aged solutions (r2/r1 ratios of 26.8 and 18.4, respectively). These differences are not considered
240     significant.

241     MRI contrast agents are usually classified as positive (T1) or negative (T2) depending on the
242     value of the r2/r1 ratio [5,11]. While T1 contrast agents present a high r1 value and low (<5) r2/r1
243     ratio [63, 64], T2 contrast agents exhibit the opposite behavior, with a high r2 value and a high (>10)
244     r2/r1 ratio. Thus, this nanomaterial can be classified as a typical T2 contrast agent, as expected.
245     Transverse relaxivities obtained for these IONPs were comparable to those that other authors have
246     reported for similar ultra-small magnetic colloids [5].

247

248     3.3 *In vivo* MRI results.

249     Following the characterization of IONPs, *in vivo* biodistribution was studied in mice with either
250     fresh IONPs solutions, used within 3 weeks after preparation, and aged solutions of IONPs, used
251     circa 9 months after preparation. As it has been already described, size, shape and physicochemical
252     properties of both solutions presented no significant differences, at the moment of use.

253     During imaging sessions, a series of anatomical images were acquired before and after the
254     injection of IONPs to properly allocate the organs of interest. Figure 4 shows a coronal view of the
255     abdomen of a mouse, where the main organs of the RES, i.e. the liver (small fragment of it visible at
256     the top of the images) and the spleen (the granular organ on the left side) are visible, together with
257     the two kidneys (bean shaped organs). Images show the abdomen of mice at two different time
258     points (before injection, BI, on the left and after injection, AI, on the right) to which a batch of aged
259     IONPs (Figure 4a) and a batch of fresh IONPs (Figure 4b) were injected. At first sight, it could be
260     visualized how the liver of the animal injected with aged solutions of IONPs darkened after
261     injection, due to the accumulation of T2 contrast agent (IONPs).

262

263
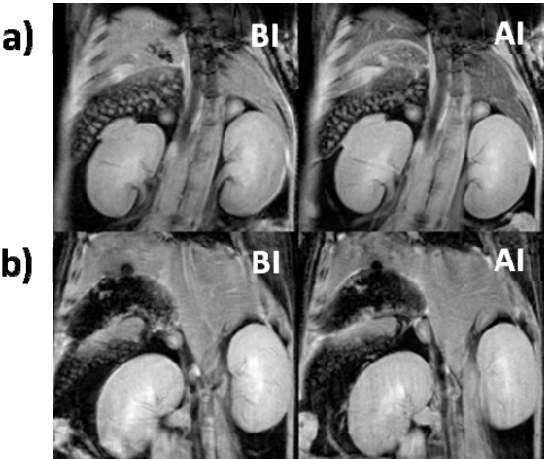
**Figure 4.** Coronal MR images of the abdominal cavity of mice before (BI) and after (AI) injection of aged (a) or freshly (b) prepared solutions of IONPs.

In order to quantify the accumulation of nanoparticles in the different organs, transversal T2 parametric maps where constructed from acquired T2 multi-echo images (see methods section). Typical T2 maps of animals, pre- and post-injection of fresh and aged solutions, are presented in figure 5, where the organs of the two principal routes of withdrawal of particles from bloodstream (RES and the urinary pathways) are visible.
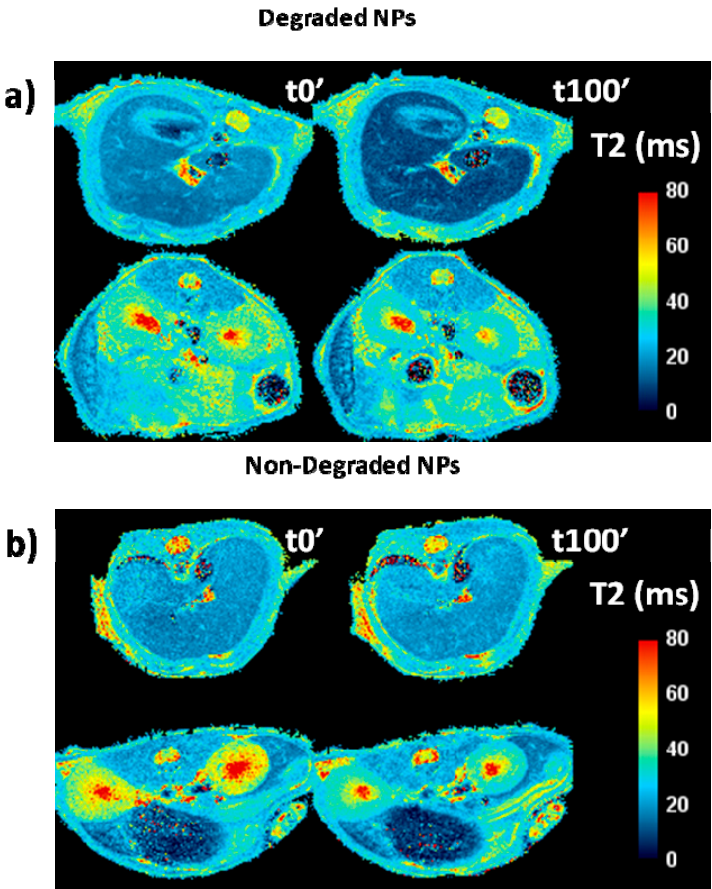


**Figure 5.** T2 relaxation maps at two different locations of the abdomen of a mouse showing the liver (top rows in both images) and the spleen and the kidneys (bottom row in both images). Two different time points are presented to reflect the changes in T2 values before (t0') and 100 minutes after (t100′) the injection of the aged IONPs (a) and fresh IONPs (b).

301    Figure 5 is representative of the two different biodistribution patterns observed in our studies.
302    For aged solutions of IONPs (panel a in figure 5) darkening of the liver and spleen indicate
303    accumulation of IONPs in the RES organs (lowering T2 values). However, for a freshly prepared
304    solution of nanoparticles (panel b in figure 5) no significant changes are observed at these two
305    organs, while the kidneys show a clear change in relaxation times.

306    Studies were performed in a group of n=6 (aged) and n=7 (fresh) animals, and T2 values where
307    measured in selected regions of interest (ROIs) for all organs, at t=20 min interval for 120 min post
308    injection of the contrast agent (giving a total experimental time of 3h including pre-contrast
309    imaging). ROI drawing was carefully performed to avoid the inclusion of regions of high T2 values
310    that usually correspond to fluids like blood (portal vein and other blood vessels in the liver, and
311    renal artery and/or vein in kidneys) or bile (gallbladder and bile ducts in the liver). In addition, two
312    different analyses were performed for the kidneys, by selecting an ROI of the whole kidney, or two
313    different ROIs, one corresponding to the medulla and the other to the cortex of the kidneys. Both
314    kidneys were analyzed separately. Plots of T2 evolution with time for all these ROIs for a
315    representative animal of each group are presented in figure 6.
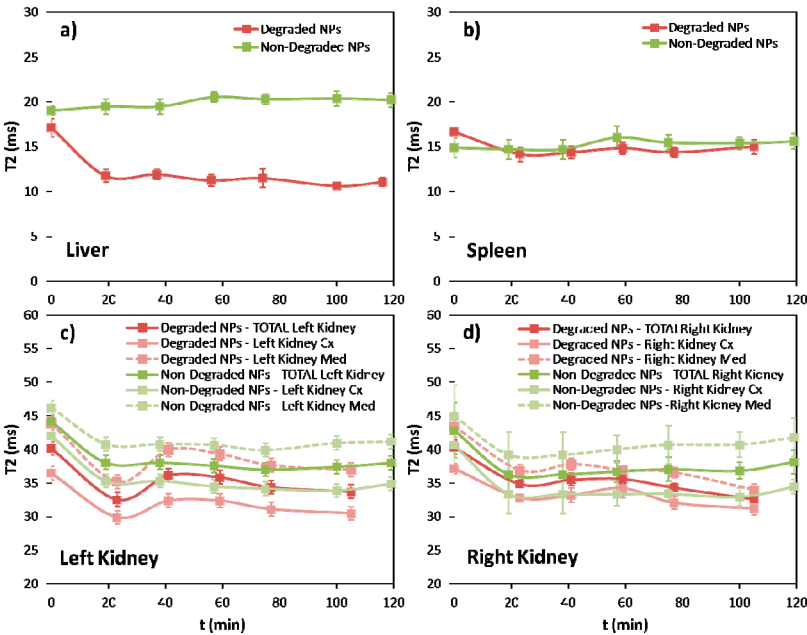


**Figure 6.** Evolution of the T2 relaxation times with time for the four different organs analyzed (liver
(a), spleen (b), left kidney (c) and right kidney (d)), after the injection of the aged solution (degraded,
red) and a freshly prepared solution (non-degraded, green) of IONPs in two representative animals
of each group.

334    Figure 6 summarizes numerically what it is visually perceptible in figure 5. When the solution
335    of nanoparticles is used during the first few weeks after solution, they are able to avoid the RES and
336    do not accumulate in the liver or spleen (green lines in figure 6a and 6b), ending up in the kidneys,
337    with preference to accumulate in their cortical region. It is noticeable that accumulation takes place
338    already during the first 20 min, and no further reduction of T2 values is observed beyond this point.
339    The drop in T2 values is higher than 20% in the kidneys. Conversely, when IONPs are injected after
340    remaining circa 9 months in solution, a considerable drop in T2 values is observed in the RES organs
341    (particularly in liver) in detriment of the kidneys, pointing to the loss of stealth capacity. Once more,
342    nanoparticle accumulation seems to take place mainly during the first 20 min post injection, and T2
343    values only experiment little changes after that point.

344     Taking into account these results, a new plot was constructed to show the mean variation of
345 relaxation times observed for each group (mean ± SD), and pooling together all the post contrast
346 points for all animals, to present the mean change observed in T2 values, pre and post contrast,
347 when fresh and aged nanoparticle solutions were used (Figure 7).

348
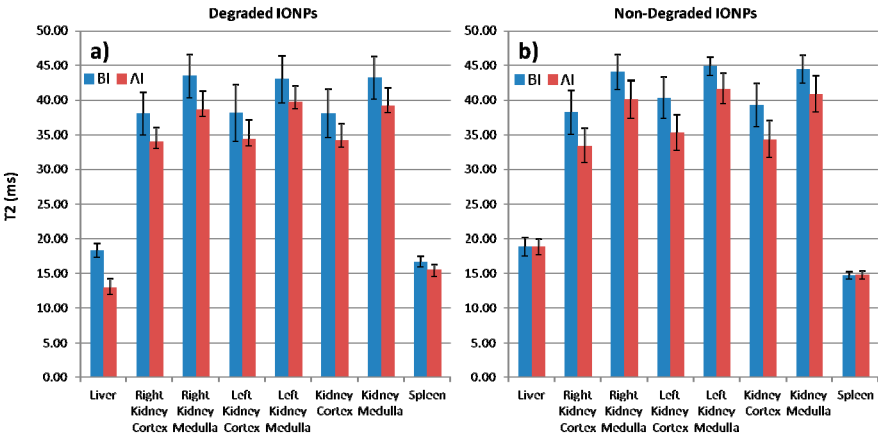


**Figure 7.** Mean (±SD) T2 relaxation values obtained for different organs before (blue) and after (red)
injection of the degraded (a) and non-degraded (b) IONPs.

360

361     The value of T2 observed for the liver pre- contrast was very consisting for animals of both
362 groups (aged, 18.3±1.0 *vs.* fresh, 18.8±1.4 ms) and with the post contrast injection value of group
363 treated with fresh nanoparticles (18.8±1.2 ms), but descend a 30% (to 12.9±1.3) after injection for the
364 group treated with aged nanoparticles. Same behavior is observed for the spleen, with values that
365 remain almost invariable for fresh nanoparticles (14.5±0.6 pre- *vs.* 14.8±0.6 ms post- contrast) but
366 decreased a 10% for the aged ones (16.7±0.8 *vs.* 15.5±0.8 ms). For the kidneys, averaged mean drops
367 of 10-13% of T2 values after injection have been observed for both groups. In global, these results
368 point to the fact that, after 9 months in solution, nanoparticles have lost their stealth capacity, which
369 is not the case for IONPs used within 3 weeks after solution.

370     These results evidenced the clear effects of NPs aging, seriously altering their biodistribution
371 and availability, as reflected in the *in vivo* MRI experiments, despite maintaining similar
372 physicochemical properties. We could demonstrate that the non-degraded or freshly prepared
373 IONPs perfectly worked as negative contrast agents for the kidneys, where they mainly
374 accumulated, inducing only minor effects in the liver and spleen, which confirms their stealth
375 capacity and low retention by the RES. On the contrary, aging of IONPs in solution seems to induce
376 some changes causing their fast uptake by the liver and spleen macrophages. Thus we further
377 investigated the nature of these changes.

378

379     3.4 Stability of the polymer coating in water: hydrolysis of ester groups

380     Based on the results of the clear evidences of the different biodistributions for the differently
381 aged IONPs, the stability of surface coating of the nanoparticles was studied with nuclear magnetic
382 resonance (NMR) spectroscopy. Polymer coating was prepared in similar conditions than those used
383 for the synthesis of the IONPs using methoxypolyethylene glycol acrylate and P4VP in deuterated
384 water. The sample was stored at room temperature and analyzed periodically by NMR
385 spectroscopy. We observed that there was a time dependent degree of hydrolysis of the ester groups
386 present in the PEG coating of the IONPs (Figure 8A shows the hydrolysis and the Retro-Michael
387 reaction and the signals of the protons that were analyzed with NMR).
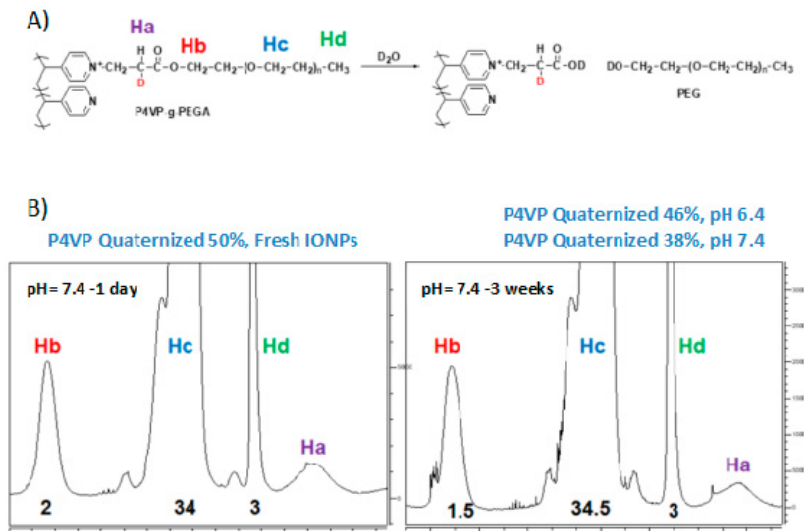
**Figure 8.** Time influence on the stability of the polymeric coating of PEG coated IONPs. (A) Hydrolysis of ester groups present on the P4VP-g-PEG IONP coating.

The intensity of the signal of the terminal methoxy group (Hd) and the methylene of the ethylene oxide repeating units (Hc) were used as reference, and compared with the intensity of the protons of the methylene group (Hb) attached to the acrylate group and the signal of proton (Ha) in the $\alpha$ position of the carbonyl group. After 3 week the degree of quaternized pyridine in the coating decrease from 50 to 38% which represents a 25 % less of grafting density when the pH of the sample was adjusted to pH 7.4. This loss is mainly due to the hydrolysis of the ester groups although the appearance of a triplet next to Hb shows also the presence of small fraction of the starting monomer due to retro Michael reaction. Sample was extracted with dichloromethane and analyses by mass spectroscopy (data not shown) settling the presence of the hydroxyl polyethylene glycol formed during the hydrolysis process. The degree of the hydrolysis was reduced just to 8% in the same period of time by adjusting the final pH of the sample to 6.4. Therefore, not only storage time, but storage conditions (e.g. pH) have a key role in the preservation of the structural, and ultimately of the biomedical, properties of IONPs. These phenomena, along with other storing strategies, such as the influence of lyophilization- resuspension cycles, need to be explored in detail (as it is taking place in our laboratories) to better understand how particles can be effectively preserved in time, for their translation to practical biomedical applications, performed far from synthetic laboratories (especially when GMP or similar grades of particles are required).

## 4. Conclusions

The use of nanomaterials, in particular IONPs, for biomedical applications is becoming very intense. The structure and physicochemical properties of these materials play a role of utmost importance in their biodistribution and availability. Several effective solutions have been proposed to increase circulation time of nanomaterials in the blood stream, avoidance opsonization and the RES, being the decoration of particles with PEG among the most common ones. However, aging of particles in solution may affect the integrity of such coating with dramatic consequences for the biomedical profile of the particles. A phenomenon that may require an in depth analysis, since regular inspection such as measurement of size, shape or superficial charge may not be sufficient to detect such phenomenon. To take actions that preserve nanoparticles' properties once synthesized is of paramount importance to ensure their potential biomedical properties [33].

**Author Contributions:** conceptualization, S. C-R., S. P-G. and P. R-C.; methodology, S. C-R., S.P-G., R. P., J. L. M., J. R-C., D. P., A. M and P. R-C.; software, S. C-R., D. P. and P. R-C.; validation, S. C-R., S.P-G., R. P., J. L. M., D. P., A. M and P. R-C.; formal analysis, S. C-R., S.P-G., R. P., J. L. M., J. R-C., D. P., A. M and P. R-C.;

433 writing—original draft preparation, S. C-R., S.P-G., A. M and P. R-C.; writing—review and editing, S. C-R.,
434 S.P-G., R. P., J. L. M., J. R-C., D. P., A. M and P. R-C.

439 **Conflicts of Interest:** The authors declare no conflict of interest.

## References

441 1.  Sánchez, A.; Ovejero Paredes, K.; Ruiz-Cabello, J.; Martínez-Ruíz, P.; Pingarrón, J.M.; Villalonga, R.; Filice,
442     M. Hybrid Decorated Core@Shell Janus Nanoparticles as a Flexible Platform for Targeted Multimodal
443     Molecular Bioimaging of Cancer. ACS Applied Materials & Interfaces 2018, 10, 31032-31043,
444     doi:10.1021/acsami.8b10452.
445 2.  Reguera, J.; Jiménez de Aberasturi, D.; Henriksen-Lacey, M.; Langer, J.; Espinosa, A.; Szczupak, B.;
446     Wilhelm, C.; Liz-Marzán, L.M. Janus plasmonic–magnetic gold–iron oxide nanoparticles as contrast
447     agents for multimodal imaging. Nanoscale 2017, 9, 9467-9480, doi:10.1039/C7NR01406F.
448 3.  Pellico, J.; Lechuga-Vieco, A.V.; Almarza, E.; Hidalgo, A.; Mesa-Nuñez, C.; Fernández-Barahona, I.;
449     Quintana, J.A.; Bueren, J.; Enríquez, J.A.; Ruiz-Cabello, J., et al. *In vivo* imaging of lung inflammation with
450     neutrophil-specific 68Ga nano-radiotracer. Scientific Reports 2017, 7, 13242,
451     doi:10.1038/s41598-017-12829-y.
452 4.  Jennings, L.E.; Long, N.J. 'Two is better than one'—probes for dual-modality molecular imaging. Chem.
453     Commun. 2009, 10.1039/B821903F, 3511-3524, doi:10.1039/B821903F.
454 5.  Kim, J.; Piao, Y.; Hyeon, T. Multifunctional nanostructured materials for multimodal imaging, and
455     simultaneous imaging and therapy. Chemical Society Reviews 2009, 38, 372-390.
456 6.  Wu, W.; Jiang, C.Z.; Roy, V.A.L. Designed synthesis and surface engineering strategies of magnetic iron
457     oxide nanoparticles for biomedical applications. Nanoscale 2016, 8, 19421-19474,
458     doi:10.1039/C6NR07542H.
459 7.  Na, H.B.; Song, I.C.; Hyeon, T. Inorganic Nanoparticles for MRI Contrast Agents. Advanced Materials
460     2009, 21, 2133-2148, doi:10.1002/adma.200802366.
461 8.  Colombo, M.; Carregal-Romero, S.; Casula, M.F.; Gutiérrez, L.; Morales, M.P.; Böhm, I.B.; Heverhagen,
462     J.T.; Prosperi, D.; Parak, W.J. Biological Applications of Magnetic Nanoparticles. Chemical Society
463     Reviews 2012, 41, 4306-4334.
464 9.  Ai, F.; Ferreira, C.A.; Chen, F.; Cai, W. Engineering of radiolabeled iron oxide nanoparticles for
465     dual-modality imaging. Wiley Interdisciplinary Reviews: Nanomedicine and Nanobiotechnology 2015, 8,
466     619-630, doi:10.1002/wnan.1386.
467 10. Pellico, J.; Ruiz-Cabello, J.; Saiz-Alía, M.; Rosario, G.; Caja, S.; Montoya, M.; Fernández de Manuel, L.;
468     Morales, M.P.; Gutiérrez, L.; Galiana, B., et al. Fast synthesis and bioconjugation of 68Ga core-doped
469     extremely small iron oxide nanoparticles for PET/MR imaging. Contrast Media & Molecular Imaging 2016,
470     11, 203-210, doi:10.1002/cmmi.1681.
471 11. Caravan, P.; Ellison, J.J.; McMurry, T.J.; Lauffer, R.B. Gadolinium(III) Chelates as MRI Contrast Agents:
472     Structure, Dynamics, and Applications. Chemical Reviews 1999, 99, 2293-2352, doi:10.1021/cr980440x.
473 12. Bhatnagar, P.; Alauddin, M.; Bankson, J.A.; Kirui, D.; Seifi, P.; Huls, H.; Lee, D.A.; Babakhani, A.; Ferrari,
474     M.; Li, K.C., et al. Tumor Lysing Genetically Engineered T Cells Loaded with Multi-Modal Imaging
475     Agents. Scientific Reports 2014, 4, 4502, doi:10.1038/srep04502
476 13. Kreyling, W.G.; Abdelmonem, A.M.; Ali, Z.; Alves, F.; Geiser, M.; Haberl, N.; Hartmann, R.; Hirn, S.; de
477     Aberasturi, D.J.; Kantner, K., et al. *In vivo* integrity of polymer-coated gold nanoparticles. Nature
478     Nanotechnology 2015, 10, 619, doi:10.1038/nnano.2015.111
479 14. Larson, T.A.; Joshi, P.P.; Sokolov, K. Preventing Protein Adsorption and Macrophage Uptake of Gold
480     Nanoparticles via a Hydrophobic Shield. ACS Nano 2012, 6, 9182-9190, doi:10.1021/nn3035155.
481 15. Zhang, G.; Yang, Z.; Lu, W.; Zhang, R.; Huang, Q.; Tian, M.; Li, L.; Liang, D.; Li, C. Influence of anchoring
482     ligands and particle size on the colloidal stability and *in vivo* biodistribution of polyethylene glycol-coated
483     gold nanoparticles in tumor-xenografted mice. Biomaterials 2009, 30, 1928-1936,
484     doi:https://doi.org/10.1016/j.biomaterials.2008.12.038.

485  16.  Wong, R.M.; Gilbert, D.A.; Liu, K.; Louie, A.Y. Rapid Size-Controlled Synthesis of Dextran-Coated,
486       64Cu-Doped Iron Oxide Nanoparticles. ACS Nano 2012, 6, 3461-3467, doi:10.1021/nn300494k.

487  17.  Gómez-Vallejo, V.; Puigivila, M.; Plaza-García, S.; Szczupak, B.; Piñol, R.; Murillo, J.L.; Sorribas, V.; Lou,
488       G.; Veintemillas, S.; Ramos-Cabrer, P., et al. PEG-copolymer-coated iron oxide nanoparticles that avoid the
489       reticuloendothelial system and act as kidney MRI contrast agents. Nanoscale 2018, 10, 14153-14164,
490       doi:10.1039/C8NR03084G.

491  18.  Wang, B.; He, X.; Zhang, Z.; Zhao, Y.; Feng, W. Metabolism of Nanomaterials *in vivo*: Blood Circulation
492       and Organ Clearance. Accounts Chem. Res. 2013, 46, 761-769, doi:10.1021/ar2003336.

493  19.  Levy, M.; Luciani, N.; Alloyeau, D.; Elgrabli, D.; Deveaux, V.; Pechoux, C.; Chat, S.; Wang, G.; Vats, N.;
494       Gendron, F., et al. Long term *in vivo* biotransformation of iron oxide nanoparticles. Biomaterials 2011, 32,
495       3988-3999.

496  20.  Karakoti, A.S.; Das, S.; Thevuthasan, S.; Seal, S. PEGylated Inorganic Nanoparticles. Angewandte Chemie
497       International Edition 2011, 50, 1980-1994, doi:10.1002/anie.201002969.

498  21.  Jin-Wook, Y.; Elizabeth, C.; Samir, M. Factors that Control the Circulation Time of Nanoparticles in Blood:
499       Challenges, Solutions and Future Prospects. Current Pharmaceutical Design 2010, 16, 2298-2307,
500       doi:http://dx.doi.org/10.2174/138161210791920496.

501  22.  Pernia Leal, M.; Rivera-Fernández, S.; Franco, J.M.; Pozo, D.; de la Fuente, J.M.; García-Martín, M.L.
502       Long-circulating PEGylated manganese ferrite nanoparticles for MRI-based molecular imaging.
503       Nanoscale 2015, 7, 2050-2059, doi:10.1039/C4NR05781C.

504  23.  Tong, S.; Hou, S.; Zheng, Z.; Zhou, J.; Bao, G. Coating Optimization of Superparamagnetic Iron Oxide
505       Nanoparticles for High T2 Relaxivity. Nano letters 2010, 10, 4607-4613, doi:10.1021/nl102623x.

506  24.  Alexis, F.; Pridgen, E.; Molnar, L.K.; Farokhzad, O.C. Factors Affecting the Clearance and Biodistribution
507       of Polymeric Nanoparticles. Molecular Pharmaceutics 2008, 5, 505-515, doi:10.1021/mp800051m.

508  25.  Briley-Saebo, K.C.; Cho, Y.S.; Shaw, P.X.; Ryu, S.K.; Mani, V.; Dickson, S.; Izadmehr, E.; Green, S.; Fayad,
509       Z.A.; Tsimikas, S. Targeted Iron Oxide Particles for *In vivo* Magnetic Resonance Detection of
510       Atherosclerotic Lesions With Antibodies Directed to Oxidation-Specific Epitopes. Journal of the American
511       College of Cardiology 2011, 57, 337-347, doi:https://doi.org/10.1016/j.jacc.2010.09.023.

512  26.  Veiseh, O.; Sun, C.; Fang, C.; Bhattarai, N.; Gunn, J.; Kievit, F.; Du, K.; Pullar, B.; Lee, D.; Ellenbogen, R.G.,
513       et al. Specific targeting of brain tumors with an optical/MR imaging nanoprobe across the blood brain
514       barrier. Cancer research 2009, 69, 6200-6207, doi:10.1158/0008-5472.CAN-09-1157.

515  27.  Cole, A.J.; David, A.E.; Wang, J.; Galban, C.J.; Hill, H.L.; Yang, V.C. Polyethylene glycol modified,
516       cross-linked starch-coated iron oxide nanoparticles for enhanced magnetic tumor targeting. Biomaterials
517       2011, 32, 2183-2193.

518  28.  Di Marco, M.; Sadun, C.; Port, M.; Guilbert, I.; Couvreur, P.; Dubernet, C. Physicochemical
519       characterization of ultrasmall superparamagnetic iron oxide particles (USPIO) for biomedical application
520       as MRI contrast agents. International journal of nanomedicine 2007, 2, 609-622.

521  29.  Fang, C.; Bhattarai, N.; Sun, C.; Zhang, M. Functionalized Nanoparticles with Long-Term Stability in
522       Biological Media. Small 2009, 5, 1637-1641, doi:10.1002/smll.200801647.

523  30.  Lartigue, L.; Alloyeau, D.; Kolosnjaj-Tabi, J.; Javed, Y.; Guardia, P.; Riedinger, A.; Péchoux, C.; Pellegrino,
524       T.; Wilhelm, C.; Gazeau, F. Biodegradation of Iron Oxide Nanocubes: High-Resolution In Situ Monitoring.
525       ACS Nano 2013, 7, 3939-3952, doi:10.1021/nn305719y.

526  31.  Pelaz, B.; Del Pino, P.; Maffre, P.; Hartmann, R.; Gallego, M.; Rivera-Fernandez, S.; de la Fuente, J.M.;
527       Nienhaus, G.U.; Parak, W.J. Surface Functionalization of Nanoparticles with Polyethylene Glycol: Effects
528       on Protein Adsorption and Cellular Uptake. ACS Nano 2015, 9, 6996-7008.

529  32.  Jokerst, J.V.; Lobovkina, T.; Zare, R.N.; Gambhir, S.S. Nanoparticle PEGylation for imaging and therapy.
530       Nanomedicine (London, England) 2011, 6, 715-728, doi:10.2217/nnm.11.19.

531  33.  Dutz, S.; Wojahn, S.; Gräfe, C.; Weidner, A.; Clement, J. Influence of Sterilization and Preservation
532       Procedures on the Integrity of Serum Protein-Coated Magnetic Nanoparticles. Nanomaterials 2017, 7, 453.